Landing Gear Noise Mitigation by an upstream installed Fairing

Gondrum, M. ; Niemöller, A. ; Meinke, M. ; Schröder, W.; Rubio Carpio, A.; Ragni, D.; Avallone, F.

DOI
10.2514/6.2022-2847

Publication date
2022

Document Version
Final published version

Published in
28th AIAA/CEAS Aeroacoustics 2022 Conference

Aeroacoustics Conferences
June 14-17, 2022, Southampton, UK
28th AIAA/CEAS Aeroacoustics 2022 Conference

10.2514/6.2022-2847

Landing gear noise mitigation by an upstream installed fairing

M. Gondrum*, A. Niemöller†, M. Meinke‡, and W. Schröder§
Institute of Aerodynamics, RWTH Aachen University, Wüllnerstr. 5a, 52062 Aachen, Germany

A. R. Carpio¶, D. Ragni‖, and F. Avallon**
Faculty of Aerospace Engineering, Delft University of Technology, Kluyverweg 1, 2629 HS Delft, The Netherlands

The time resolved flow and acoustic fields around a simplified two-wheel nose landing gear configuration featuring brakes, torque link, and a detachable fairing are investigated by numerical and experimental means. The flow field is computed by a lattice Boltzmann method with a collision step based on countable cumulants. Numerical near field flow predictions are validated by experimental results from Delft University of Technology. The comparison shows the quality of the applied computational setup and methodology. The favorable noise mitigation properties of the installed fairing are discussed.

I. Introduction

The reduction of the perceived aircraft noise level during take-off and approach is becoming more and more important due to increasingly stringent regulations. Aircraft noise originates from the engine mainly generated by the jet and the fan, and airframe noise mostly arising from high lift devices and landing gears (LG). During approach and landing, the noise contribution from the airframe becomes significant, since engines are operated almost under idle conditions. The focus of this study is on the prediction of landing gear noise and its mitigation by a fairing installation. Due to the various blunt LG sub-components, a separated turbulent flow field is generated, whose interaction with downstream LG elements is responsible for broadband noise generation [1]. The LG noise mitigation by the installed fairing is predicted and analyzed by a numerical method based on a lattice Boltzmann method. A simplified LG geometry including torque links and brakes is used. Several numerical studies on the LAGOON nose LG configuration defined in the AIAA Benchmark problems for Airframe Noise Computations (BANC) have been conducted previously, see [2–5]. The results of these studies helped to understand the various noise generation mechanisms, e.g., by cavity effects in the wheels, but they did not investigate strategies for noise mitigation. The installation of LG fairings to reduce the noise level has been investigated recently in [6], promising a high potential for real aircraft application.

In the present study, the aeroacoustic field around two configurations of a two-wheel nose LG is investigated. The first is a baseline configuration, whereas the second geometry is characterized by a solid flat fairing attached in front of the LG with the intention to alter the turbulent flow field around the sub-components. In contrast to the numerical study in [7], a more simplified geometry at lower wind tunnel Reynolds numbers and considerably higher mesh resolution is considered. The results of the present study serve as a first step for analyzing fairings composed of various porous materials replacing the solid material in subsequent investigations conducted within the framework of the European project INVENTOR.

The remainder of this work has the following structure: First, the applied computational methodology, i.e., the cumulant lattice Boltzmann method method, is presented. In section III.B details of the LG geometry, flow conditions, and the experimental and computational setup are provided. A grid resolution study and an analysis of the flow and acoustic field are discussed in section IV.

II. Computational methodologies

The turbulent flow field and the acoustic near field is predicted by a lattice Boltzmann (LB) method with a collision step based on countable cumulants [8]. The method is implemented in the multiphysics solver framework m-AIA, which

*Research Scientist, RWTH Aachen University, m.gondrum@aia.rwth-aachen.de.
†Research Scientist, RWTH Aachen University.
‡Senior Scientist, RWTH Aachen University, AIAA member, m.meinke@aia.rwth-aachen.de.
§Professor, RWTH Aachen University, AIAA member, office@aia.rwth-aachen.de.
¶Research Scientist, Delft University of Technology.
‖Associate Professor, Delft University of Technology, AIAA member.
**Associate Professor, Delft University of Technology, AIAA member.

is developed at the Institute of Aerodynamics of RWTH Aachen University.

A. Cumulant lattice Boltzmann method

The Boltzmann equation describes the evolution in time t of the momentum distribution function $f(\boldsymbol{x}, \boldsymbol{v}, t)$

$$\frac{\partial f}{\partial t} + \boldsymbol{v} \cdot \nabla f = \Omega(f), \tag{1}$$

with f representing the density of particles at the position $\boldsymbol{x}$ and time t with a velocity $\boldsymbol{v}$, and the collision operator Ω as its source term accounting for the effect of the momentum exchange of particle collisions on the distribution function. Enskog demonstrated [9] through a series expansion of the momentum distribution function with the perturbation parameter ϵ, i.e., $f = f^{(0)} + \epsilon f^{(1)} + O(\epsilon^2)$, that a first-order approximation of the Boltzmann equation recovers the Navier-Stokes equations.

The lattice Boltzmann equation is obtained by discretizing eq. (1):

$$f_i(\boldsymbol{x} + c_i \Delta t, t + \Delta t) = f_i^*(\boldsymbol{x}, t) = f_i(\boldsymbol{x}, t) + \Omega_i(f),$$

with $c_i = v_i/\sqrt{3}$ denoting the discrete particle velocity in the discrete direction i. The asterisk $(*)$ indicates the post-collision state. In the present study, the particle velocity space is discretized in a three-dimensional Cartesian lattice featuring 27 discrete velocity directions. Macroscopic flow quantities such as the density ρ and the flow velocity $\boldsymbol{u}$ are obtained from the moments of the momentum distribution function. These read in discrete form

$$\rho(\boldsymbol{x}, t) = \sum_i f_i(\boldsymbol{x}, t) \quad \text{and} \quad \boldsymbol{u}(\boldsymbol{x}, t) = \frac{1}{\rho} \sum_i \boldsymbol{c}_i f_i(\boldsymbol{x}, t)\,.$$

The collision step, i.e., calculating the value of the collision operator, is often described by the Bhatnagar-Gross-Krook (BGK) operator [10]

$$\Omega_i = \omega_{BGK}[f_i^{eq} - f_i],$$

with f_i^{eq} being the Maxwell equilibrium distribution function and ω_{BGK} being the non-dimensional relaxation frequency

$$\omega_{BGK} = \frac{\Delta t c_s^2}{\nu_{eff} + \frac{1}{2}\Delta t c_s^2},$$

where Δt denotes the time step and ν_{eff} the effective viscosity representing the sum of the fluid viscosity, a turbulent viscosity calculated by a Smagorinsky sub-grid scale model [11], and an artificially viscosity introduced in a sponge region close to the domain boundaries to damp reflected waves.

In the present study, the collision procedure of Geier et al. [8] is applied. In contrast to the BGK procedure it is well suited for high Reynolds number flow. Instead of relaxing the momentum distribution function towards an equilibrium state in momentum space, so called countable cumulants are relaxed, which are observable quantities that are Galilean invariant and statistically independent of each other. Therefore, the particle distribution function transformed in the cumulant space c_α is collided before being transformed back into momentum space

$$c_\alpha^* = c_\alpha + \omega_\alpha[c_\alpha^{eq} - c_\alpha],$$

where c_α^{eq} is the Maxwellian equilibrium in cumulant space, and ω_α is the relaxation frequency. Following the nomenclature of [8], all relaxation rates but ω_1 are set to unity

$$\omega_1 = \omega_{BGK}\,, \qquad \omega_\alpha = 1: \quad \alpha \neq 1\,.$$

The propagation step, i.e., scattering the post-collision distribution to the neighboring lattice, as well as boundary conditions are performed in momentum space after transforming the post-collision cumulants back into momentum space. To reduce computational effort local grid refinement is implemented by using the method of Dupuis and Chopard [12]. Therefore, the relaxation time varies between the different levels of refinement. To account for weak compressibility effects an acoustic scaling is conducted such that the computational time step scales with the grid spacing $\Delta t \sim \Delta$.

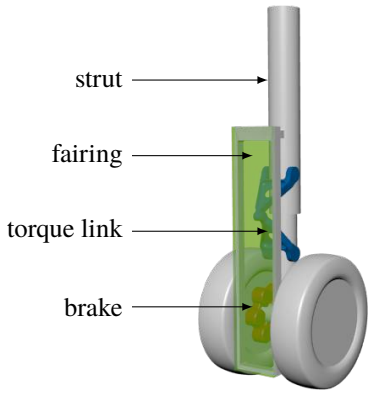

Fig. 1 Landing gear including brakes (red), torque link (blue), and fairing (green), which can be replaced by different materials. Each feature including the fairings' holder is removable.

Table 1 Geometry and flow parameters.

Wheel diameter D	150 mm
Upper strut diameter	0.24 D
Distance axle-wall	2.33 D
Outer wheel base	0.95 D
Fairing to strut distance	0.37 D
Fairing height	1.8 D
Fairing width	0.36 D
Mach number M_∞	0.10198
Wheel Reynolds number Re_D	346,306
Upper strut Reynolds number Re_S	83,113
Inflow turbulence intensity (exp.)	< 0.06 %

III. Landing gear configuration and computational setup

A simplified two-wheel nose landing gear (LG), featuring brakes, a torque link, and a detachable fairing, as shown in fig. 1 is considered in this study. The wheel diameter is $D = 150$ mm approximately corresponding to a 1:7 scale real nose LG. The fairing used for noise mitigation is placed 0.37 D in front of the strut having a height of 1.8 D and a width of 0.36 D. It covers the torque link, parts of the brakes and the lower strut. The LG is attached to a solid flat plate at a distance of 2.7 D to the outlet nozzle. The setup is investigated at a freestream Mach number of $M_\infty = 0.10198$ and a wheel based Reynolds number of $Re_D = 343,306$ with an inflow turbulence intensity below of 0.06 %. Table 1 summarizes the geometric parameters and the flow conditions.

A. Experimental setup

The experiments are conducted in the open-jet closed-circuit vertical aeroacoustic wind tunnel (A-Tunnel [13]) at Delft University of Technology (TUD), which has an extent of $6.4 \times 6.4 \times 3.2\ m^3$. The LG model is attached to a flat plate in a distance of 2.7 D to the exit of the rectangular nozzle *Delft 40x70*, which is 2.7 D width and 4.7 D height. The flow field is investigated in a plane parallel to the flat plate behind the LG's axle with the dimension of $1.2 \times 1.6\ D^2$. Therefore, particle image velocimetry (PIV) measurements using a *La Visison Imager sCOMOS CLHS* camera at a frame rate of 15 Hz being placed 1 m away of the plane of interest are conducted. The flow is made visible by a vaporized mixture of water and glycol with mean droplet diameter of 1 μm seeded by a *SAFEX* fog generator and illuminated with a *Quantel Evergreen II* laser.

Acoustic data are recorded with a microphone array composed of 64 *G.R.A.S. 40PH* free-field microphones distributed over a planar ellipse with major-to-minor axis ratio of 2 and a major effective diameter of 2 m. With a flat frequency response ($\pm 1\ dB$) within 10 Hz to 20 kHz, the microphones allow for a maximum input of 135 dB ($re\ 20\ \mu Pa$). The array is arranged for a flyover and a sideline measurement in a distance of 7 D and 9 D to the LG's axle, respectively. In both setups the array center is shifted by 1.46 D in mean flow direction compared to the LG's axle. Data are recorded for 20 s at a sampling frequency of 51.2 kHz. The experimental setup is shown in fig. 2.

B. Computational setup

The computational setup is shown in fig. 3. It has a total extent of $130D \times 65D \times 32.5D$ including the sponge layer, where no artificial viscosity is added in a region of $80D \times 40D \times 20D$. The LG is attached to a slip wall one third of the domain length distant from the inflow boundary condition. On the LG's surface a no-slip wall boundary condition is applied using a second-order accurate interpolated bounce-back scheme. The in- and outflow are represented by non-reflecting characteristic boundary condition (CBC) as introduced by Izquierdeo and Fueyo [14] extended into three space dimensions. These are based on solving the local one-dimensional inviscid (LODI) equations, which resemble the Euler equations without transverse terms, to mitigate waves being reflected back into the domain. The obtained macroscopic state is set through the associated microscopic equilibrium state. A pressure boundary condition is applied

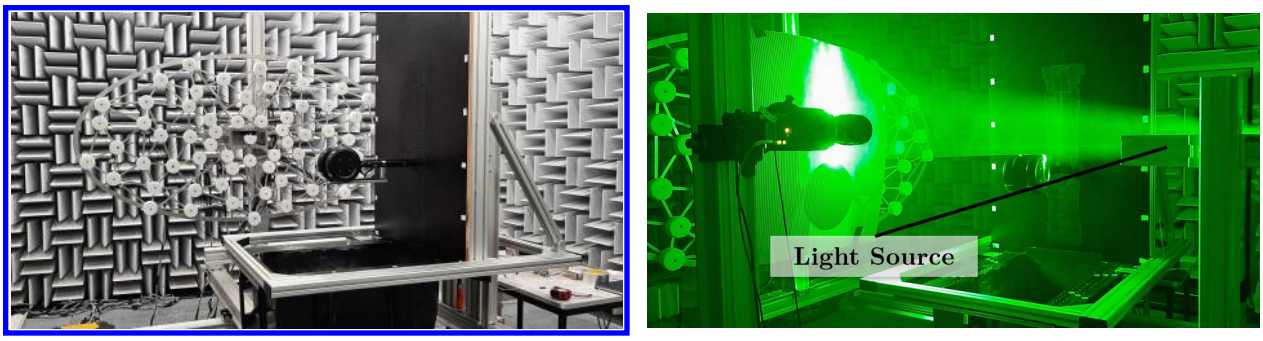

Fig. 2 Experimental setup conducted at TUD's A-Tunnel with the outlet nozzle *Delft 40x70* [13] blowing in top wise direction. The landing gear shown features the installed fairing, whereas the microphone array is positioned sideline. On the right hand side the setup during image acquisition is shown.

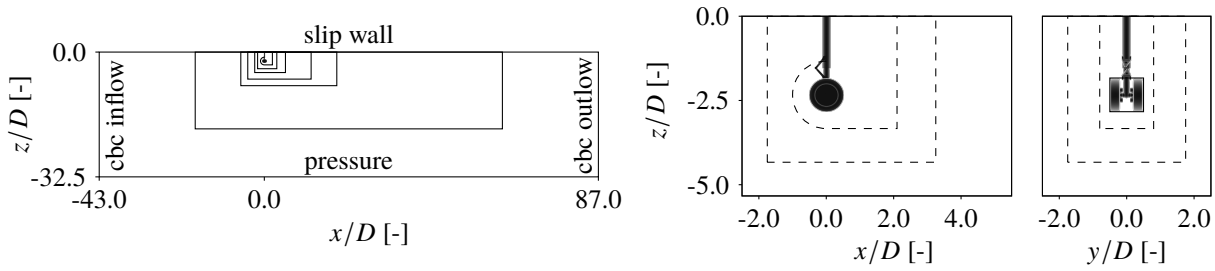

Fig. 3 Numerical setup of the cumulant LB flow simulation. 2D slices showing the dimension of the refinement patches in black lines (–). The patches in dashed lines (-·) are not used in the coarse grid. On the left, a slice of the complete domain starting with a refinement level of 9 is shown. The two figures on the right show details starting with a refinement level of 13.

to all other surfaces, i.e., the velocity is extrapolated from the domain's interior while the pressure is fixed to ambient condition.

The spacing of the Cartesian grid on the refinement level r is given by $\Delta x_r = L/2^r$, where Δx_0 represents the bounding box of the computational domain with a length of $L = 130\ D$. Starting from a minimum refinement level of $r_{min} = 9$ the grid is refined at each refinement patch shown in fig. 3 by one level. Additionally, a boundary fitted refinement with a thickness of $0.02\ D$ on the maximum refinement level is applied on the LG's surface transitioning to the next patch refinement level with at least 10 cells per layer, see fig. 4. Three grids with increasing maximum refinement level summarized in table 2 are considered in a grid resolution study.

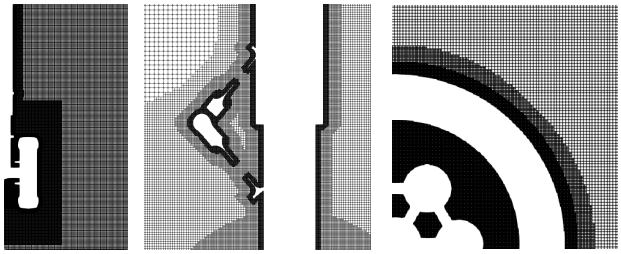

Fig. 4 Details of the grid refinement around the wheel, torque link, and brakes for the grid with medium resolution.

Table 2 Properties of the CFD grids in the grid convergence study.

Grid	noCells/D	dt [s]	noCells
coarse	252	1e-06	150 million
medium	504	5e-07	200 million
fine	1008	2.5e-07	705 million

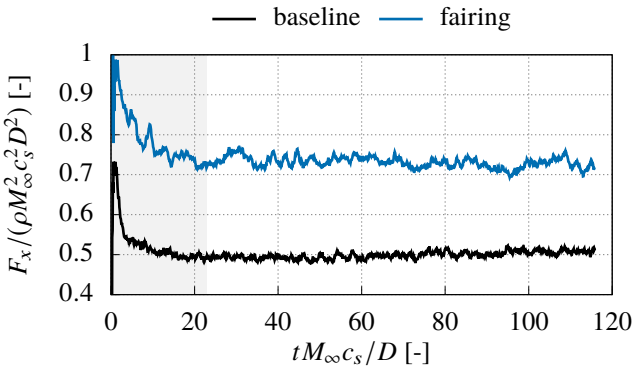

Fig. 5 Temporal evolution of the aerodynamic drag force acting on the baseline (–), and the baseline with fairing (–) configuration. Additionally, the time period which is neglected in averaging and sampling the flow field is shaded in gray.

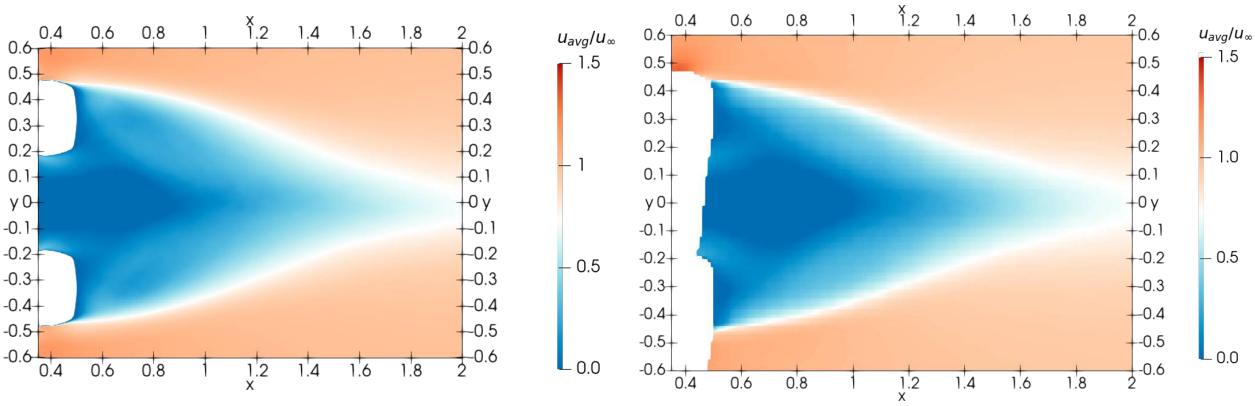

Fig. 6 Mean velocity field of the component in the main flow direction around the baseline configuration. On the left-hand side, the result of the fine grid resolution and on the right-hand side the experimental measurements are given. The slice is positioned at $z = z_{axle}$ with a normal in the z direction.

IV. Results

A. Grid convergence study

The flow fields computed by three increasingly higher grid resolutions are compared to data obtained from experimental measurements. The three grids are characterized in table 2 and fig. 3. The turbulent flow field is averaged for a period of 93 D/u_∞ corresponding to 0.4 s in the experiment to get a converged mean flow field. Hereby, the recording is started after the transient phase of 22 $D/u\infty$. The effect of the developing flow field is well seen in the temporal evolution of the aerodynamic drag force acting on the LG as shown in fig. 5. A slice of the mean velocity field in the main flow direction $\overline{u}$ through the LG's wake is given in fig. 6 comparing the numerical results based on the fine grid resolution to the experimental data. It is visible that the shape of the wake agrees well with the measured flow field indicating a sufficient mesh resolution. A detailed probing of the u field is given in fig. 7, where two profiles of the streamwise velocity component in the wake region are depicted. The first profile is chosen along the x-direction in the symmetry plane, while the second is placed perpendicular to the first one in the $z = z_{axle}$ plane 1.17 D downstream of the LG's axle. Aside from the mean values $\overline{u}$ the root mean square (RMS) values of the perturbed velocity field $RMS(u')$ are given for each of the three resolutions and the experimental data. For both quantities on both lines a better agreement with the experimental data can be observed for increasing grid resolution. With the fine grid resolution the RMS values are predicted reasonably well aside from the centerline in the near wake region, where somewhat higher RMS values are seen in the numerical solution.

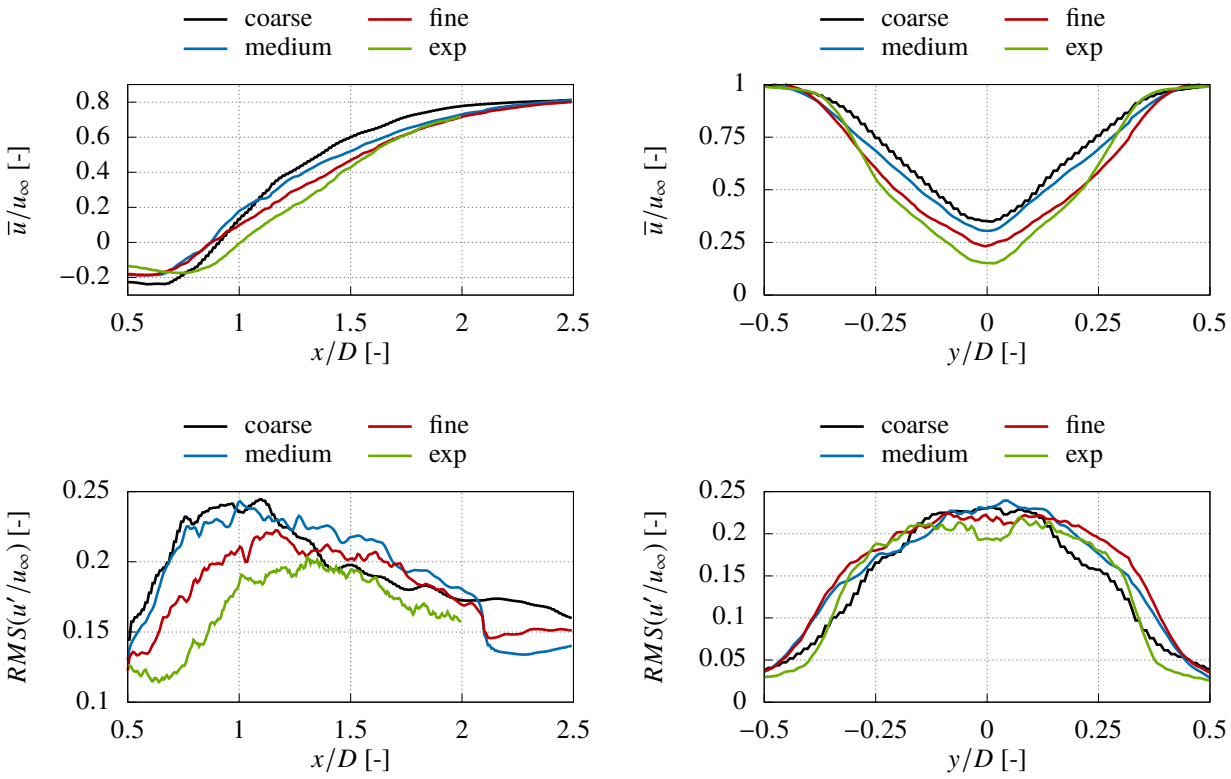

Fig. 7 Comparison of the mean (top) and RMS (bottom) values of the velocity component in the main flow direction between the three grid resolutions and the experimental data. Results are shown on a line with $y = 0, z = z_{axle}$ (left) and on a line with $x = 1.17\ D, z = z_{axle}$ (right).

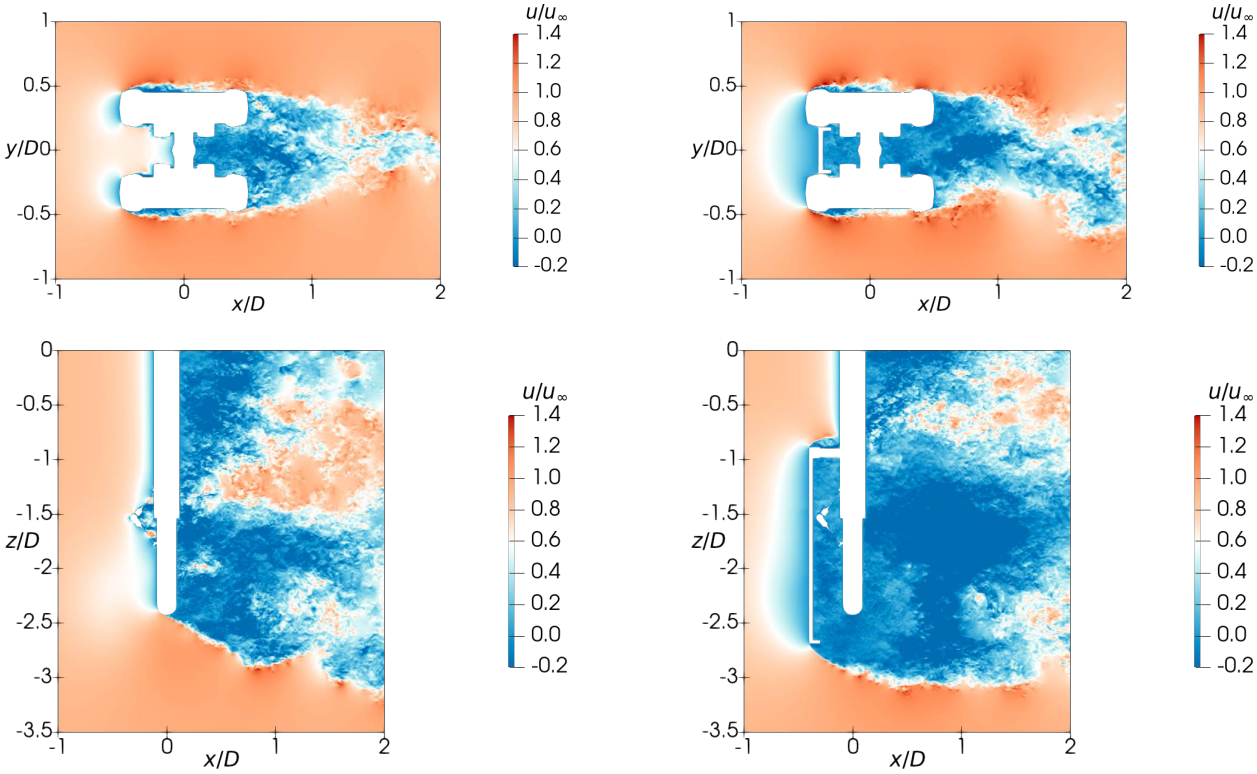

Fig. 8 Contours of the instantaneous velocity field of the velocity component in the main flow direction around the baseline LG (left) and the LG with fairing (right). The first slice (top) is positioned at $z = z_{axle}$ with a normal in the z direction. The second slice (bottom) is positioned in the symmetry plane.

B. Near field results

The instantaneous velocity fields of the two configurations, i.e., the baseline LG and the LG with attached fairing are shown in fig. 8. It is visible that the wake flow field is quite different for the two cases. The case with the fairing shows a larger low velocity region in the symmetry plane between the wheels and around the torque link significantly reducing the wake of the torque link hitting on the strut. These observations agree with the computed drag of the two configurations in fig. 5, showing that the fairing introduces a drag increase of approximately 40 % compared to the baseline LG configuration. The directly resolved perturbed pressure field $p' = p - \overline{p}$ predicted by the LB solver is given in fig. 9. Here, the pressure field is shown in a region with a grid refinement level corresponding to more than five points per wave length of an acoustic wave associated to a frequency of 20 kHz. The acoustic field is looking smooth round the landing gear. It is observable that the amplitude lateral of the wheels and in the wake is increased for the configuration with fairing. In this configuration the wave pattern in front of the LG in the region of $x/D < -2$ is less ordered and of smaller amplitudes indicating destructive interference.

C. Far field results

Spectra of the sound pressure level (SPL) between 100 Hz and 10 kHz measured in the acoustic far field at a lateral and a flyover position as described in section III.A are shown in fig. 10 for the two configuration, i.e., baseline and baseline with fairing. For the baseline configuration the SPL is decreasing towards higher frequencies, whereas three regions indicate an increased SPL at 300 Hz, 1000 Hz, and between 3 kHz and 5 kHz. For the modified configuration with attached fairing these three regions are not observable. The SPL is slightly increased below of 200 Hz and clearly decreased by 5 dB to 10 dB in the frequency range of 1 kHz to 10 kHz.

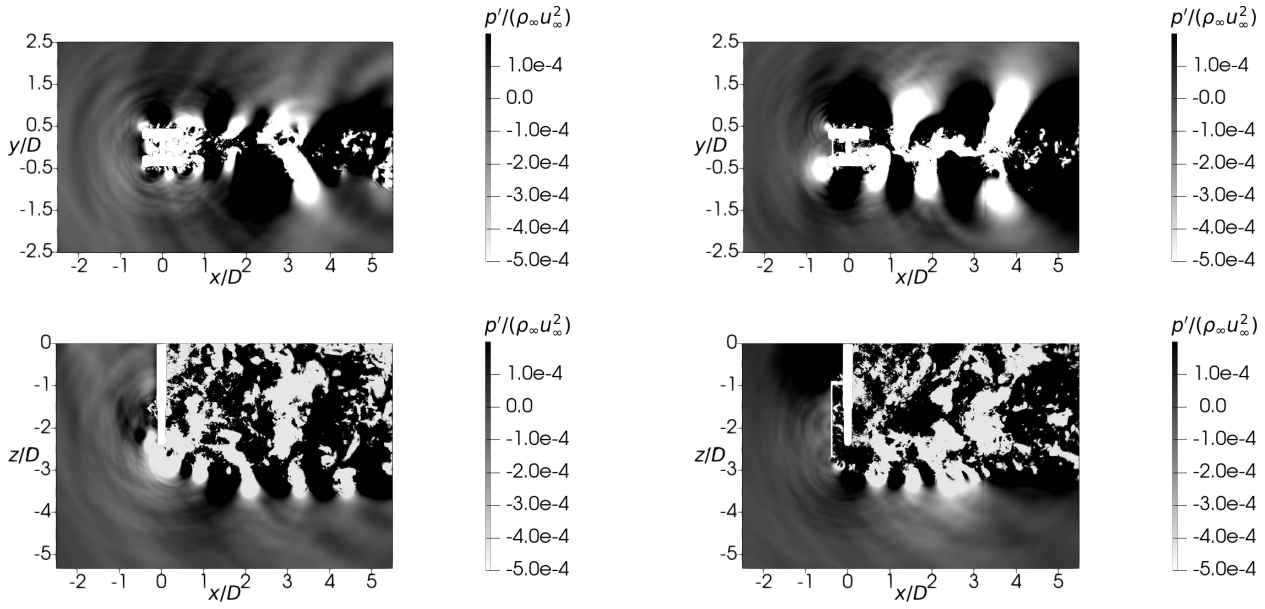

Fig. 9 Instantaneous perturbed pressure field p' around the baseline (left) and the baseline with fairing (right) configuration. The first slice (top) is positioned at $z = z_{axle}$ with a normal in the z direction. The second slice (bottom) is positioned on the symmetry plane. The data are calculated on a grid refinement level of at least 13.

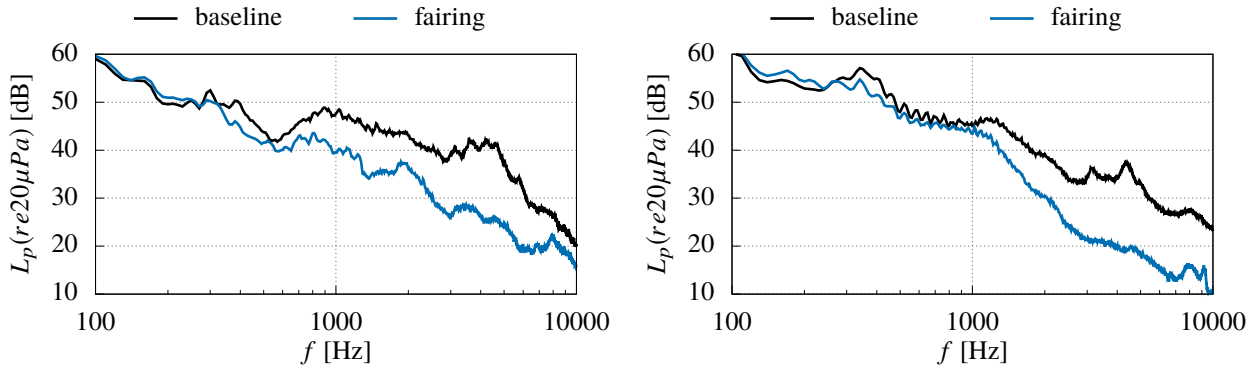

Fig. 10 Sound pressure level generated by the baseline (–) and the baseline with fairing (–) configuration measured at the center microphone for the flyover (left) and sideline (right) setup.

V. Conclusion and outlook

In the present study it has been shown that a geometrical simple fairing installed upstream of a two-wheel nose LG has favorable noise mitigation effects over a wide frequency range in the order of 5 *dB* to 10 *dB*. A computational setup based on cumulant lattice Boltzmann method has been presented and validated against experimental measurements. To obtain a deeper understanding of the favorable noise mitigation effects acoustic far field data will be provided by computational aeroacoustics methods such as Ffowcs-Williams and Hawkings method. Correlating these results with the well-resolved acoustic near field obtained by the given computational setup will help to identify the dominant noise sources that are mitigated by the installed fairing.

Acknowledgments

The project received funding from the European Union's Horizon 2020 research and innovation programme within the project INVENTOR (*innovative design of installed airframe components for aircraft noise reduction*) listed under the grant agreement ID: 860538.
The authors gratefully acknowledge the Gauss Centre for Supercomputing e.V. (www.gauss-centre.eu) for funding this project by providing computing time on the GCS Supercomputer HAWK at Höchstleistungsrechenzentrum Stuttgart (www.hlrs.de).

References

[1] Dobrzynski, W., "Almost 40 Years of Airframe Noise Research: What Did We Achieve?" *J. Aircraft*, Vol. 47, No. 2, 2010, pp. 353–367. https://doi.org/10.2514/1.44457.

[2] Ricciardi, T. R., Wolf, W. R., and Speth, R., "Acoustic Prediction of LAGOON Landing Gear: Cavity Noise and Coherent Structures," *AIAA J.*, Vol. 56, No. 11, 2018, pp. 4379–4399. https://doi.org/10.2514/1.J056957.

[3] Casalino, D., Ribeiro, A., Fares, E., and Nölting, S., "Lattice–Boltzmann aeroacoustic analysis of the LAGOON landing-gear configuration," *AIAA J.*, Vol. 52, No. 6, 2014, pp. 1232–1248. https://doi.org/10.2514/1.J052365.

[4] Casalino, D., Ribeiro, A., and Fares, E., "Facing rim cavities fluctuation modes," *J. Sound Vibr.*, Vol. 333, No. 13, 2014, pp. 2812–2830. https://doi.org/10.1016/j.jsv.2014.01.028.

[5] Sanders, L., Manoha, E., Khelil, S., and Francois, C., *LAGOON: New Mach Landing Gear Noise Computation and further analysis of the CAA process*, 2012. https://doi.org/10.2514/6.2012-2281.

[6] Zhao, K., Okolo, P., Neri, E., Chen, P., Kennedy, J., and Bennett, G., "Noise reduction technologies for aircraft landing gear-A bibliographic review," *Prog. Aerosp. Sci.*, Vol. 112, 2020, p. 100589. https://doi.org/10.1016/j.paerosci.2019.100589.

[7] Murayama, M., Yokokawa, Y., Yamamoto, K., and Hirai, T., "Computational study of low-noise fairings around tire-axle region of a two-wheel main landing gear," *Comput. Fluids*, Vol. 85, 2013, pp. 114–124. https://doi.org/10.1016/j.compfluid.2012.11.001, international Workshop on Future of CFD and Aerospace Sciences.

[8] Geier, M., Schönherr, M., Pasquali, A., and Krafczyk, M., "The cumulant lattice Boltzmann equation in three dimensions: Theory and validation," *Comp. Math. Applics*, Vol. 70, No. 4, 2015, pp. 507–547. https://doi.org/10.1016/j.camwa.2015.05.001.

[9] Enskog, D., "Kinetische Theorie der Vorgänge in mässig verdünnten Gasen." Ph.D. thesis, 1917.

[10] Bhatnagar, P. L., Gross, E. P., and Krook, M., "A Model for Collision Processes in Gases. I. Small Amplitude Processes in Charged and Neutral One-Component Systems," *Phys. Rev.*, Vol. 94, 1954, pp. 511–525. https://doi.org/10.1103/PhysRev.94.511, URL https://link.aps.org/doi/10.1103/PhysRev.94.511.

[11] Hou, S., Sterling, J., Chen, S., and Doolen, G., "A Lattice Boltzmann Subgrid Model for High Reynolds Number Flows," *Fields Instsitute Communication*, Vol. 6, 1996, pp. 151–166.

[12] A., D., and Chopard, B., "Theory and applications of an alternative lattice Boltzmann grid refinement algorithm," *Phys. Rev. E*, Vol. 67, 2003, p. 066707. https://doi.org/10.1103/PhysRevE.67.066707, URL https://link.aps.org/doi/10.1103/PhysRevE.67.066707.

[13] Merino-Martínez, R., Rubio Carpio, A., T.Lima Pereira, L., van Herk, S., Avallone, F., Ragni, D., and Kotsonis, M., "Aeroacoustic design and characterization of the 3D-printed, open-jet, anechoic wind tunnel of Delft University of Technology," *Applied Acoustics*, Vol. 170, 2020, p. 107504. https://doi.org/10.1016/j.apacoust.2020.107504.

[14] Izquierdo, S., and Fueyo, N., "Characteristic nonreflecting boundary conditions for open boundaries in lattice Boltzmann methods," *Phys. Rev. E*, Vol. 78, 2008, p. 046707. https://doi.org/10.1103/PhysRevE.78.046707.